ADVANCED FUNCTIONAL MATERIALS
www.afm-journal.de

# In Situ TEM Investigation of the Lithiation and Delithiation Process Between Graphene Sheets in the Presence of Atomic Defects

*Yueliang Li, Felix Börrnert, Mahdi Ghorbani-Asl, Johannes Biskupek, Xuemei Zhang, Yongsheng Zhang, Dominic Bresser, Arkady V. Krasheninnikov, and Ute Kaiser**

**Using advanced in situ transmission electron microscopy, the lithiation and delithiation processes into graphene sheets are studied and significant differences are detected in the structural evolution of the system. Thin *fcc* lithium crystals with faceted shapes are formed between graphene sheets during lithiation, but are transformed into irregular patches during delithiation. It is found that defects such as vacancies in graphene and impurity atoms play the key role in these processes. Specifically, during intercalation the lithium crystals nucleate at vacancies in graphene, while upon delithiation the impurity oxygen atoms initially embedded at octahedral interstitial positions inside the lithium crystals agglomerate at the edges of the crystals, thus giving rise to the formation of amorphous lithium oxide patches, where lithium ions are trapped.**

## 1. Introduction

The global demand for lithium-ion batteries (LIBs) has increased dramatically in the last ten years due to the explosive growth of the electric vehicle market.[1,2] Despite extensive research focusing on improving performance such as energy and power density, LIBs suffer from capacity loss and resistance increase, leading to both energy and power fade during usage.[3] Numerous studies have been carried out to understand the failure mechanisms of LIBs in order to improve their lifetime.[4] The fading of LIBs is a consequence of many factors,[5] such as the continuous growth of the solid electrolyte interphase layer,[6,7] lithium plating,[8] degradation of the positive electrode,[9,10] and particle fracture in both electrodes.[11] Crystal defects have been proven to play a critical role in all these factors.[12–15] For example, defects can create hot spots of locally high electrochemical activity, which can lead to lithium plating at the negative electrode.[16] Moreover, capacity loss and current leakage resulting from the decomposition of the electrodes and electrolyte are affected by the size and position of the defects.[17] However, defects do not always have a detrimental effect on the LIB operation. The aliovalent substitution of $Fe^{3+}$ for $Zn^{2+}$ in ZnO anodes can lead to the formation of local defects such as cationic vacancies, which serve as potential sites for an initial $Li^+$ ion insertion, thus, favouring the lithiation kinetics.[18–20] Defects can also relieve strain between two phases during phase transformations in spinel $Li_xMn_2O_4$ cathode materials.[21,22] Therefore, defect engineering has become an important approach to design the electrochemical properties and performance of electrode materials.[14,23]

Among the crystal defects that can influence the functionality of battery materials are impurity atoms in substitutional and

Y. Li, F. Börrnert, J. Biskupek, U. Kaiser
Electron Microscopy Group of Materials Science
Ulm University
89081 Ulm, Germany
E-mail: ute.kaiser@uni-ulm.de
Y. Li, D. Bresser
Helmholtz Institute Ulm
89081 Ulm, Germany

The ORCID identification number(s) for the author(s) of this article can be found under https://doi.org/10.1002/adfm.202406034



**DOI: 10.1002/adfm.202406034**

Y. Li, D. Bresser
Karlsruhe Institute of Technology (KIT)
76021 Karlsruhe, Germany
F. Börrnert
CEOS GmbH
Englerstraße 28, 69126 Heidelberg, Germany
M. Ghorbani-Asl, X. Zhang, A. V. Krasheninnikov
Institute of Ion Beam Physics and Materials Research
Helmholtz-Zentrum Dresden-Rossendorf
01328 Dresden, Germany
X. Zhang
Science Island Branch of Graduate School
University of Science and Technology of China
Hefei 230026, China
Y. Zhang
Advanced Research Institute of Multidisciplinary Sciences
Qufu Normal University
Qufu, Shandong 273165, China

interstitial positions, as well as vacancies. These defects can appear at the stage of materials synthesis, during electrochemical cycling,[24] high temperature operation,[25] or irradiation[21] when the battery is used in extreme environments, such as cosmic space.

While defects in inorganic materials and their impact on the de-/lithiation process have been in the focus of recent research, [26] the impact of defects in graphite as the state-of-the-art anode material of today's LIBs[27] has attracted significantly less attention. First-principles calculations,[28] in fact, indicate that vacancies in graphene sheets strongly affect the intercalation energetics and diffusion barriers of Li atoms. Greatly enhanced capacities were also observed experimentally in disordered and porous graphitic structures, thus, further highlighting the need to better understand the impact of such defects for graphite and other graphitic materials.[29,30]

To understand the effects that crystal defects may have on battery electrode materials, atomic-scale imaging is one of the most suitable tools. Recently, we succeeded in imaging the lithiation and delithiation processes between sheets of bilayer graphene at the atomic scale by using chromatic and spherical aberration-corrected high-resolution transmission electron microscopy ($C_C/C_S$-corrected HRTEM).[31,32] These previous experiments also verified that the lithiation can only occur between graphene sheets and not on top or underneath of single-layer graphene (for testing lithium was placed in addition on top of single layers with no effect after biasing).[31] The graphene layers also have to fully cover the lithium, larger holes result in a fast outgassing of the lithium into the vacuum.[32] We found that in bilayer graphene, lithium adopts an ultrathin and super dense close-packed phase with an in-plane lattice parameter of 3.1 Å, not the typical $LiC_6$ phase observed after intercalation of lithium cations into graphite. In fact, the presence of such superdense lithium appears feasible only due to the possibility of graphene to sufficiently expand in the vertical direction, which is suppressed in graphite owing to required mechanical deformation of a larger number of graphene sheets. Nonetheless, an in-depth understanding of the underlying processes might help to better understand also the lithiation and delithiation processes occurring in graphite, while simultaneously providing guidelines for further improved capacities in advanced active materials such as nanostructured carbons that provide sufficient space in their crystal structures.

In this study, we thus extend our previous work by a detailed TEM analysis supported by electron energy loss spectroscopy and density functional theory calculations. We are focusing on the role that atomic defects (such as carbon vacancies in graphene and foreign oxygen atoms in the growing Li crystal) may have during cycling between graphene sheets. We observe how ultrathin lithium crystals nucleate and grow, and how impurities inside the Li crystal can affect the delithiation process. The resulting insights may be essential for gaining an in-depth understanding of the role of defects during charging and discharging processes in LIBs.

## 2. Results and Discussion

The setup for carrying out biasing and cycling experiments in the electron microscope is described in our previous paper.[32]

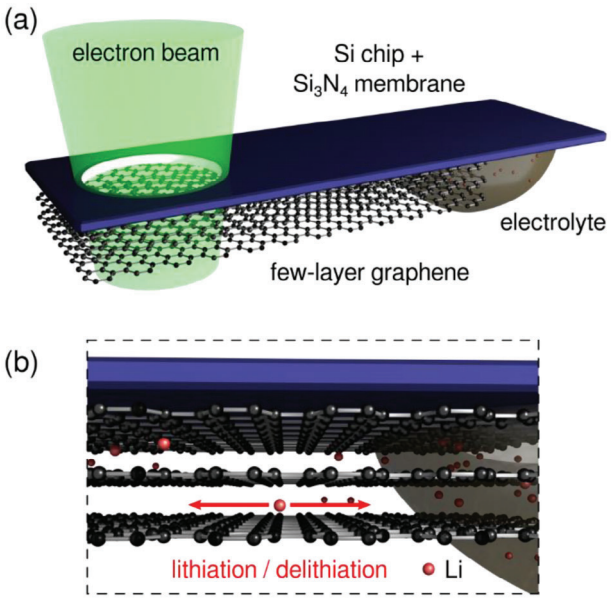


**Figure 1.** Schematic of the set-up of our graphene device. The graphene sheets are under the chip inside the microscope because the sample holder is turned by 180° when being inserted into the column of the microscope.

We report on the evaluation of data obtained for bi- and also trilayer graphene to extend the system more toward graphite. We find that the behavior of lithiation and delithiation is the same for the bi- and trilayer devices, which will be shown in detail below. **Figure 1** shows a schematic of the setup where the graphene sheets are placed freely suspended over the holes in the $Si_3N_4$ membrane. A drop of a solid polymer electrolyte covers one edge of the graphene. For the detail on the custom-designed TEM sample carrier chip we refer to ref. [32]. The de-/lithiation experiments (a positive voltage $U_G$ of 5 V is applied to insert Li ions into the graphene sheets, while $U_G = 0$ V is applied for the subsequent delithiation) were performed in situ in the chromatic- and spherical aberration-corrected ($C_C/C_S$) SALVE (Sub-Angstrom Low-Voltage Electron microscopy) instrument operated at 80 kV.[33] (See the Experimental Section).

**Figure 2** presents a sequence of the images recorded during the first-cycle lithiation process (bilayer system) and a subsequent delithiation process (trilayer system). The Li crystals grow with faceted shapes during lithiation (Figure 2a), while during delithiation they do not simply shrink in shape but transform into unfaceted irregular structures (Figure 2b). Before the lithiation starts ($t = 0$ s, Figure 2a), the pristine graphene is rather free of contamination. The inserted Fourier transform pattern confirms the presence of graphene (lattice constant of $a = 2.46$ Å). Already after 5 s of cycling, many Li nucleation seeds are formed and identified by their dark contrast (one dark patch is marked by the white arrow), their density is estimated as ca. 0.02 $nm^{-2}$ (see the Experimental Section). When the lithiation progresses further, the Li seeds grow into larger ultrathin crystalline plates with faceted shape (most of them have a triangular shape) and merge with each other. The arrows in Figure 2a mark the same Li crystal at different times of the lithiation. The inset in the image recorded at $t = 93$ s shows the corresponding Fourier

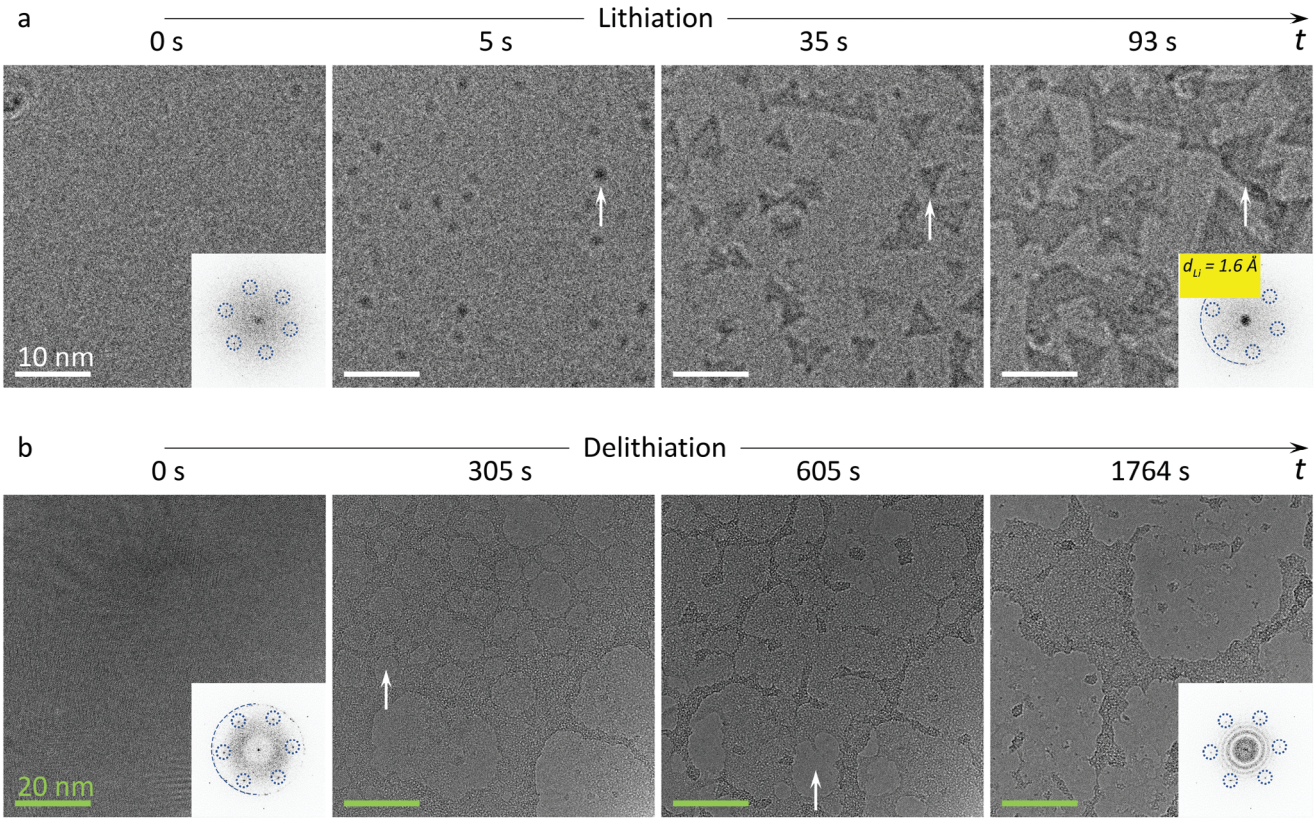


**Figure 2.** An overview image of lithiation and delithiation between graphene sheets. a) A series of TEM images showing the first-cycle lithiation process in bilayer graphene. A large underfocus is used to increase the contrast of the Li crystals. Before the lithiation ($t$ = 0 s), the inset Fourier transform shows only graphene reflections. Li crystals start to nucleate at $t$ = 5 s. From 35 s to 93 s, the Li seeds grow into larger faceted plates. The arrows mark the same Li crystal. The inset Fourier transform of the image recorded at $t$ = 93 s shows the reflections of a super dense Li phase (marked by the half ring, representing a real-space periodicity of 1.6 Å). b) A series of TEM images of a delithiation process. The inset Fourier transform of the image recorded before the delithiation shows both Li and graphene reflections. After the delithiation starts, deintercalation and shrinking of the Li crystals (darker contrast) are observed. The arrows mark the deintercalation of Li in two different interlayers. The inset Fourier transform of the image at the final state shows no Li reflection but broader rings, indicating the amorphous state of the residuals. (Scale bars of equal size are colored identically but labeled only once.).

transform where only the second order reflections of the Li phase[32] can be seen; however the first order reflections are missing. The reason for the latter extinction after evaluating the actual crystal structure of the ultrathin close-packed lithium phase will be discussed later, as we would first like to discuss the lithiation process. The whole process in a larger field of view can be seen in Video S1 with a frame interval of 2 s; in each frame, the coverage of Li crystals is measured by the ratio of the area of the Li crystals divided by the area of the field of view, and thus the growth rate was estimated (see Figure S1, Supporting Information). As seen, the growth rate of the Li crystals is rather constant with time and results in $5.2 \pm 0.1 \times 10^{-3}$ $s^{-1}$. This value is related to the Li diffusion in graphene,[30] which cannot be directly measured in our experiment due to the limited field of view. According to the measured growth rate of the Li crystals, the field of view is filled by Li within ≈3 min. If the lithiation progresses further when 2D Li crystals have already completely filled the lateral space between the graphene, the Li grains grow vertically, stretching the space between the graphene sheets. Figure S2 (Supporting Information) shows an image after the vertical growth of the Li crystals. The strong diffraction contrast and the moiré patterns indicate large (ca. 20–30 nm) and thick Li grains. Note that the vertical growth happens only after a very long lithiation process and added for completeness. However, in the following discussion we focus only on 2D Li without considering the subsequently vertically grown structures.

In our previous publication[32] the Li crystals formed outside the field of view and the growth of the crystals expanded into the field of view. Therefore, only the growth of coalesced grains was recorded. In the present work, as shown in Figure 2a, the Li crystals nucleated inside the field of view, so their behavior in the early stages of lithiation, such as nucleation, growth, and coalescence of Li nanocrystals, could be directly observed and therefore better understood.

Figure 2b shows an overview image of a delithiation process within a trilayer-graphene. To minimize irradiation damage, the lithiation was carried out without continuous simultaneous imaging but "off-screen", thus this sample in Figure 2b is not identical to that of Figure 2a (this sample could not be used for delithiation because of damage during 2 h of HRTEM imaging). At the beginning (time index t = 0 s) the field of view is fully filled by 2D Li from the previous lithiation cycle and now the

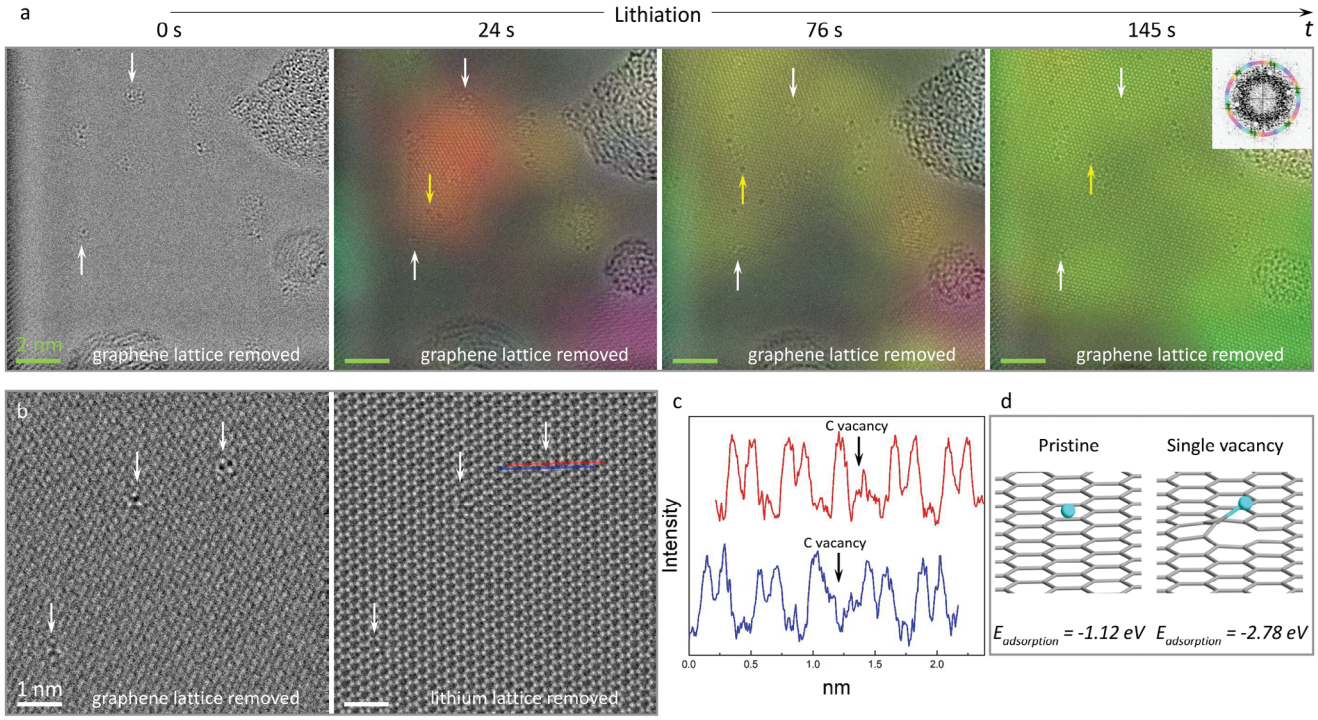


**Figure 3.** Observing lithiation at atomic scale. a) A series of $C_C/C_S$-corrected HRTEM images acquired during a lithiation experiment, with bilayer graphene lattice removed by Fourier filter. The white arrows mark the C vacancy defects in graphene. The yellow arrows mark some foreign O atoms inside the Li crystal. Colored orientation maps of Li crystals are obtained and overlaid on the images by applying a colored bandpass mask to the second order reflections of Li in the Fourier transforms (see the inset Fourier transform). b-left) Another graphene removed HRTEM image containing the contrast of the C vacancy defects marked by the arrows. b-right) The same image as the left but with Li lattice removed, leaving the graphene lattice. c) Extracted line profiles from (b). d) Calculated configurations of interaction between graphene and an isolated Li atom (left: Li adsorption on pristine graphene, right: Li adsorption on single vacancy).

delithiation was started by setting the voltage $U_G$ to 0 V. The inset Fourier transform shows clearly the reflections of metallic Li, confirming the presence of crystalline Li between the graphene sheets. When the delithiation begins, the Li crystals become disordered and shrink gradually (darker contrast). A difference to the lithiation process is clearly observed: the solid Li phase has now irregular edges and no facets. The final state of the delithiation process after ≈30 min ($t$ = 1764 s) shows residual Li-containing patches. As seen in the inserted Fourier transform no Li reflection but broader rings indicate an amorphous state of the residual material. The whole delithiation process viewed in a larger field of view can be seen in Video S2.1.

The arrow in Figure 2b at $t$ = 305 s marks the deintercalation of Li within one interlayer, while the arrow at $t$ = 605 s marks the deintercalation within the other one (at $t$ = 605 s, only a few remaining patches are still visible in the first interlayer). This observation evidences that Li is intercalated into both interlayers of the trilayer graphene. Compared to Figure 7 which shows the delithiation process in bilayer graphene, the Li atoms exhibit the exact same behavior inside trilayer graphene during delithiation except for the diffusion rate. A lithiation process inside trilayer graphene is also shown in Video S3, where faceted Li crystals grow in both interlayers successively. Therefore, we confirm that the behavior during lithiation and delithiation is the same for the bi- and trilayer devices. The data which best show the lithiation and delithiation process were used in Figure 2, independent of the number of graphene layers. One general challenge of direct imaging lithiation or delithiation behavior especially in the very first moments of the processes such as the nucleation, is the random nature when they occur. The visible area (a ≈200 nm hole in the SiN support film) is relatively small to the whole dimensions of the chip including variations of the size of the Li droplet and distance to the area of observation (some tens of µm). As a consequence, the sample has to be imaged constantly with the side effect of electron irradiation damage. We observed time intervals of few minutes for a full lithiation, but almost 2 h for the much more complex defect-determined delithiation.

In another set of experiments, we evaluated the TEM images taken during lithiation and delithiation at higher magnification to determine what role atomic defects may play in the different behavior. **Figure 3**a shows a series of $C_C/C_S$-corrected HRTEM images recorded during another lithiation experiment inside bilayer graphene, where the graphene lattice is removed by filtering in each image by Fourier filtering (see Figure S3, Supporting Information). The removal of the regular crystal lattice reflection of graphene has the positive side effect that lattice defects in graphene are recognised very easily as additional contrast. Before the lithiation starts ($t$ = 0 s), no Li crystal lattice can be observed. However, we easily recognise dark spots (two examples are marked by the white arrows), which we will later identify as single vacancies in the graphene lattice (see below). At $t$ = 24 s, already a few Li nanocrystals are visible. As the lithiation proceeds,

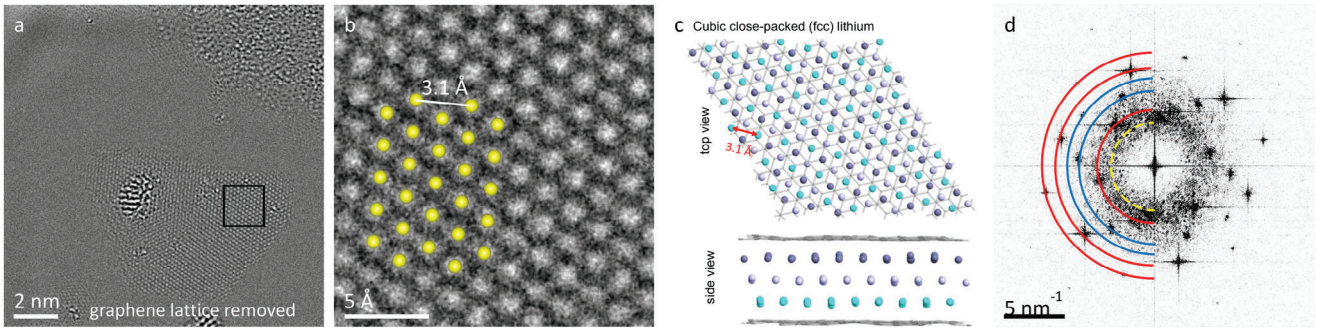


**Figure 4.** The *fcc* phase of lithium. a) an atomic-resolved Li crystal with graphene lattice removed, showing bright-atom-contrast. b) Magnified view of the boxed area in (a). c) The top view and the side view of the configuration of *fcc* Li. d) Fourier transform of (a). The red half rings mark the reflection of graphene, while the blue solid ones mark that of Li. The yellow dash half ring marks the missing 1st order reflections of Li.

the crystals grow with different orientations, and then merge into one single crystal at $t = 145$ s. This can be easily seen as the crystals are colour-coded according to their orientation.[34] The corresponding-coloured mask can be seen in the inserted FFT (fast Fourier transform) in the very right image in Figure 3a (see also the Experimental Section). The typical size of the individual Li grains is ≈20–30 nm (compare Figure S2, Supporting Information). Therefore, we can suppose the following lithiation process: very small (several nm) Li nanocrystals adjust their orientation and merge into larger (until ≈20–30 nm) crystals. When the larger (≈20–30 nm) crystals grow further and get in contact with each other, grain boundaries form. In fact, such "critical" size of the Li grains (≈20–30 nm) is in good agreement with the observation in our previous work.[32] In addition to the appearance of the Li crystals, point defects are observed during the lithiation process. We already noticed these defects in graphene at $t = 0$ s. At $t = 24$ s, the Li crystals cover these point defects, indicating that Li crystals begin to form at these point defects. All point defects originating in graphene maintain their positions during the lithiation process (as marked by the white arrows in Figure 3a). To identify the nature of the point defect, we show in Figure 3b two versions of one HRTEM image; three identical point defects are marked in both versions. In the left image, the graphene lattice is removed so that only the Li lattice is visible, while in the right image, the Li lattice is removed so that the atomically resolved graphene lattice (with bright-atom-contrast) remains. The line profiles of the image intensity of the graphene lattice in Figure 3b are extracted as shown in Figure 3c. As can be seen, one carbon atom is missing in the graphene lattice. Therefore, we have identified the point defect as a carbon vacancy.

We note that in our experiments the concentration of vacancies in the graphene – Li system is much higher than in isolated graphene sheets studied by TEM.[35,36] To understand the reason for this, we carried out DFT calculations of the vacancy formation energy using the energy of an isolated carbon atom and a carbon atom in Li-C molecules as a reference (see Figure S4, Supporting Information). It is evident that the energy penalty is much lower, as expected. Although these are the results of static calculations, the energy barrier for creating a vacancy should also be lower when a displaced recoil carbon atom interacts with nearby Li atoms present in the system, and formation of new bonds makes the displacement process energetically less costly.

DFT calculations also confirm that vacancies in graphene can act as nuclei for the growth of Li crystals as the presence of undercoordinated atoms at point defect site enhances the interaction between Li atoms with the graphene lattice (Figure 3d). The calculated adsorption energy of Li on the single vacancy is −2.78 eV, while the energy gain regarding adsorption of Li on pristine graphene is ≈1.7 eV. Similar behavior has also been reported for the interaction of Li into graphene with double vacancies.[37] However, the adsorption of Li atom on a single vacancy is energetically more favorable than on double vacancies.

Another type of atomic defects, seen in Figure 3a, shows dark contrast (marked by the yellow arrows) and was not seen in the pristine graphene before the lithiation. Such defects always appeared at the position of the Li atomic columns in all the lithiation experiments; these defects seem to be related to the Li crystal structure. Therefore, we first want to understand the stacking order of the close-packed Li, before unravelling the nature of this type of defects.

**Figure** 4a shows another atomically resolved HRTEM image of a small faceted Li crystal (the graphene lattice is removed). Figure 4b is a magnified view of the framed region in Figure 4a, showing clearly the Li lattice with sixfold symmetry. The distance between two next-nearest-neighbor atomic columns is 3.1 Å, which is in good agreement with the earlier result.[32] Each Li atomic column has 6 nearest neighbors. Figure 4c shows the *fcc* model with *ABC* stacking (*A, B, C* positions are shaded differently) between two graphene sheets (grey); above in top view along the [111] zone axis and below in side view. The top view projection agrees well with the experimental view and thus characterises the *fcc* system rather than the *hcp* (in an *hcp* system, each atomic column has only three nearest neighbours in the [0001] projection). HRTEM image simulations are presented in Figure S5 (Supporting Information) for *fcc* Li along [111] and *hcp* Li along [0001] directions with 1–6 atomic Li layers. As can be seen, an agreement between experimental and simulated images is only given for the *fcc* Li with a thickness of 3 or 6 layers. Further evidence that Li crystallises in the *fcc* structure is the extinction of the first order reflections. Figure 4d shows the Fourier transform of the raw data of Figure 4a (Li and graphene reflections are present). The spatial frequencies of the 1st to 3rd order reflections of graphene are marked by three red half rings, while those of the 2nd and 3rd order of the Li are marked by two blue solid half rings. The 1st order reflections of the Li crystal

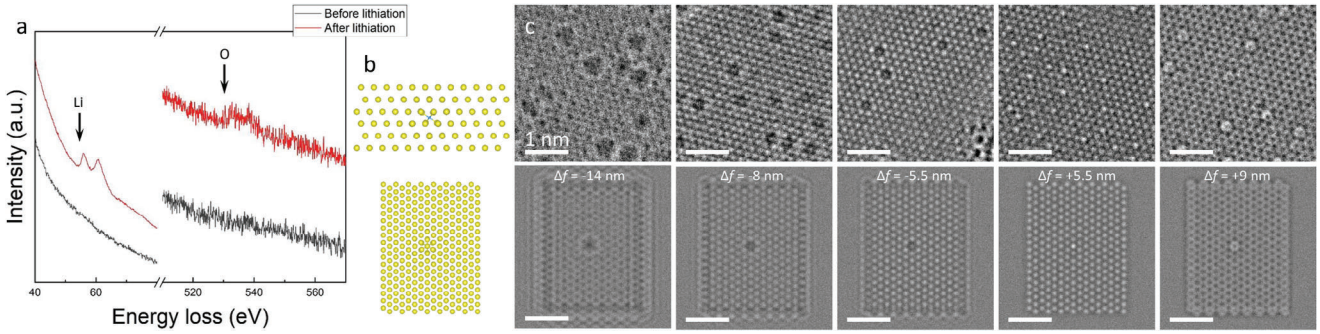


**Figure 5.** Foreign O atoms inside *fcc* Li. a) EELS spectra acquired before and after lithiation. Both an obvious Li signal and a weak O signal are seen after the lithiation. b) Atomic model of an O atom at the octahedral interstitial position inside *fcc* Li relaxed by the DFT optimisation, with the side view above and the top view below. c) Experimental HRTEM images containing O atoms recorded with different defoci and the corresponding simulated images (electron dose $1 \times 10^5$ $e^-$Å$^{-2}$) using the model in (b) as input. The defocus values are listed, respectively.

at the spatial frequency of 3.7 nm$^{-1}$ (the yellow dash half ring) are missing. Fourier transforms of each HRTEM simulation are calculated and shown in Figure S5 (Supporting Information). It can be seen that all the Fourier transform patterns are very similar except for those marked by the yellow boxes, which lack the 1st order reflections for *fcc* Li with 3 or 6 atomic layers. In conjunction with the HRTEM simulation and the fact that the 1st order reflections of the Li crystals are missing in the Fourier transforms in Figures 2–4, it can be concluded that the crystal structure of Li between the graphene layers is *fcc* (*ABC* stacking, and not hexagonal with *AB* stacking). After carefully comparing experiment and calculation, we identify in Figure 4a a thickness gradient from the top left to the bottom right corner from 3 to at least 6 single-layer Li. In most of our HRTEM images, stable Li layers with multiple of three (or six layers) were observed. However, as mentioned above, depending on the duration of the lithiation processes, we also observed Li grains that were much thicker due to vertical growth at the very late stage of the lithiation process (see Figure S2, Supporting Information). Based on our measurement of the first visible reflection in the experimental Li image with a spatial frequency of 6.3 nm$^{-1}$, indexed 220 in an *fcc* system along <111> zone axis, we determine the lattice constant of the Li crystals between graphene sheets as 4.4 Å, in agreement with that reported in the literature for *fcc* Li.[37] Our DFT calculations with the PBE functional report a lattice constant of 4.33 Å for bulk *fcc* Li, which will be used for further calculations later on.

As already mentioned, we observed the appearance of the single atomic defects with dark contrast in the Li lattice. Some examples are marked by the yellow arrows in Figure 3a. First, we find by HRTEM simulation that the defect is not a single Li vacancy (see Figure S6, Supporting Information). The comparison suggests that the defect should be a heavier foreign atom. We speculate that these atoms may be introduced together with the Li ions during lithiation. To identify the nature of the foreign atoms, local electron energy-loss spectroscopy (EELS) data were acquired before and after lithiation (**Figure 5a**). When comparing the two spectra, a Li signal is seen after lithiation, confirming the insertion of Li ions during the lithiation. Moreover, a weak oxygen K-edge signal is observed after lithiation, indicating that the heavier foreign atoms introduced during lithiation are oxygen. To understand the interaction of the foreign O atoms with *fcc* Li between graphene sheets, DFT calculations were performed with O atoms placed between graphene but outside the Li crystal. The result suggests that the O atoms prefer to be "sucked" into the Li crystal instead of being located between the graphene layer and the Li slab. The behavior is similar to C atoms implanted into Cu foils reported by Riikonen et al.[39] Calculations[37] indeed show that, of the two possible interstitial positions in an *fcc* crystal,[40] O atoms prefer the octahedral one because its formation energy is lower than the other. The atomic model with an O atom in octahedral interstitial position, shown in the side and top view in Figure 5b, is used as the input data for the subsequent HRTEM simulation. Figure 5c presents experimental HRTEM images recorded with different defoci containing the defects (top row) and the corresponding simulated images (bottom row). The contrast of an interstitial O atom in the simulated images with different defocus matches very well that of the defects in the experimental images. The defocus values are proven to be correct by other experimental images with larger field of view, containing amorphous nanoparticles as reference for the determination of the defocus (see Figure S7, Supporting Information). Thus, the single atomic defects with dark contrast are confirmed to be foreign O atoms located at the octahedral interstitial positions inside *fcc* Li. Given the experimental setup, it appears most likely that the O atoms originate either from the electrolyte or the lithium metal counter electrode, which is known to commonly comprise traces of oxygen (amongst others). (See Supporting Information for the estimation of the concentration of oxygen.)

After identifying the nature and position of the defects, we analyzed how they affect the shape of Li crystals during lithiation and delithiation, respectively. As discussed above, during lithiation, foreign O atoms are randomly located inside the Li crystals at octahedral positions. We never found them near the edge of the Li crystals. In fact, the edges are clean during lithiation (see Figures 3a and 4a). Therefore, the faceted shape of the Li crystals during lithiation should be governed by edge and interface energies. The analysis of the TEM images of the Li crystals indicates that one of the (111) Li surfaces is oriented parallel to the graphene sheets.

To rationalise the observations, we calculated the surface energies of different possible surfaces of *fcc* Li crystals with low indices, see **Figure 6a** and **Table 1**, which proved to be in good agreement with the previously reported values.[41,42] Interestingly

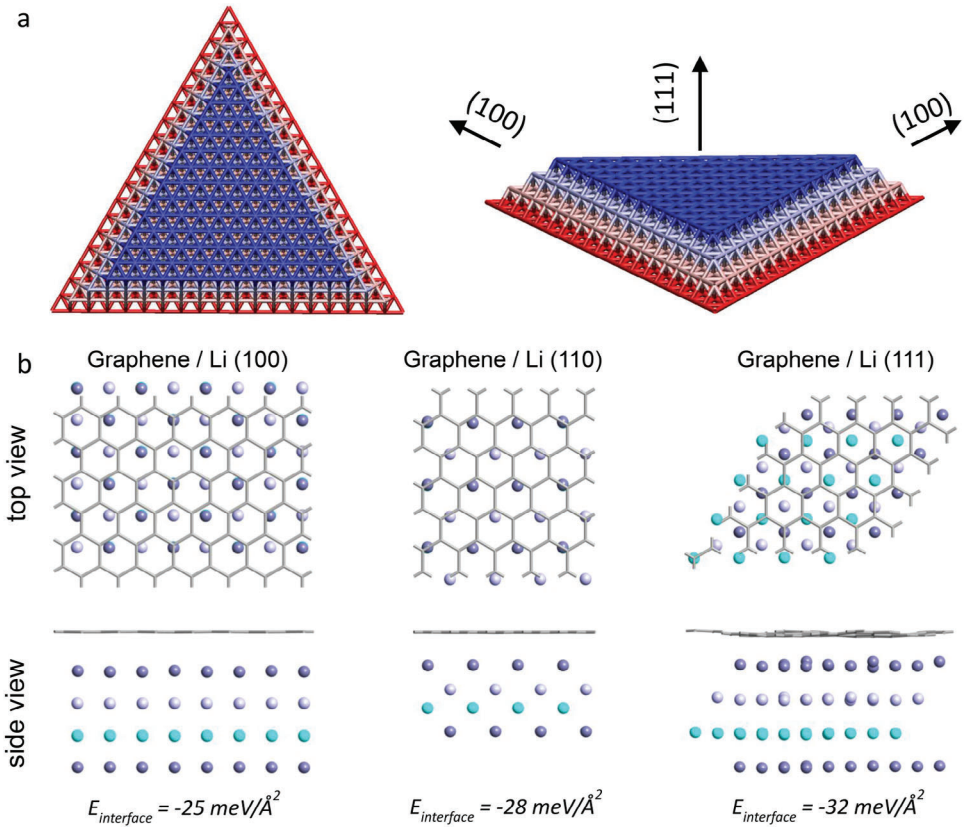


**Figure 6.** a) Top view and perspective view of a triangular Li cluster. The Li atoms are coloured according to their z-coordinate. b) The simulation model of the graphene/Li (111) interface was constructed using a 5 × 5 graphene supercell on top of a (111) 4 × 4 × 4 Li slab, with a total strain of ~0.47%, containing 114 atoms. For the graphene/Li (100) interface, the structure includes using a 7 × 2 graphene supercell on top of a (100) 4 × 2 × 4 Li slab, with a total strain of ~0.54%, containing 60 atoms. In the case of graphene/Li (110) interface, the model represents a 5 × 2 graphene supercell on top of a (100) 4 × 2 × 4 Li slab, with a total strain of ~0.68%, including 36 atoms.

enough, our calculations indicated that the (111) surface is the highest in energy. To explain this contradiction, one should also consider the energy of the interface between graphene and Li crystal, which can partially compensate for the energy penalty upon surface creation (with regard to the infinite slab). The calculation setup is presented in Figure 6b. The interface between the (111) Li surface and graphene is energetically most favorable (Table 1), and a sum of the interface and surface energies is the smallest, indicating that this type of the interface must form. The edges then should be represented by (100) surfaces, which in turn have the lowest formation energy, so that the whole picture is consistent.

During delithiation, the position of the impurity O atoms changes. **Figure** 7a shows a series of HRTEM images recorded during another delithiation process inside bilayer graphene (the graphene lattice is removed and the orientation maps of Li are overlaid). The edges of the Li phase in each image are marked by the white dotted lines. The image series shows clearly that the Li phase shrinks (as the coloured area decreases), which is associated with the transfer of the Li ions back into the electrolyte during the delithiation. The edges of the Li phase are jagged and no facets can be found, although most part of the Li phase is still crystalline. Figure 7b shows magnified views of the boxed areas in Figure 7a, and it is clearly seen that many O atoms (a few examples are marked by the arrows) gather at the edges of the Li crystal, forming a ca. 1 nm thick oxidized surface layer. Thus, the Li crystal shows no facets during the delithiation. The reason for this observation is presumably a relatively fast (interstitial) oxygen diffusion in the lithium metal, as observed for other metals,[43] and the thermodynamically favorable formation of lithium oxide at the surface of the lithium crystal, at which electrons are released when the lithium is oxidized. As the delithiation proceeds in time, the Li crystals shrink further as the foreign O atoms move together and are located inside the shell. The oxidized surface areas merge at a certain time, forming residual $Li_xO_y$, as marked by the arrows in Figure S8 (Supporting Information). From the Fourier transform in Figure 2b it is seen that the residual $Li_xO_y$ is amorphous. It should be noted that there is already $Li_xO_y$

**Table 1.** Surface energies of Li fcc crystals and interface energies of the surfaces facing graphene.

| Li Surface | Surface energy, meV Å$^{-2}$ | Interface energy, meV Å$^{-2}$ |
|---|---|---|
| 100 | 30 | −25 |
| 110 | 31 | −28 |
| 111 | 34 | −32 |

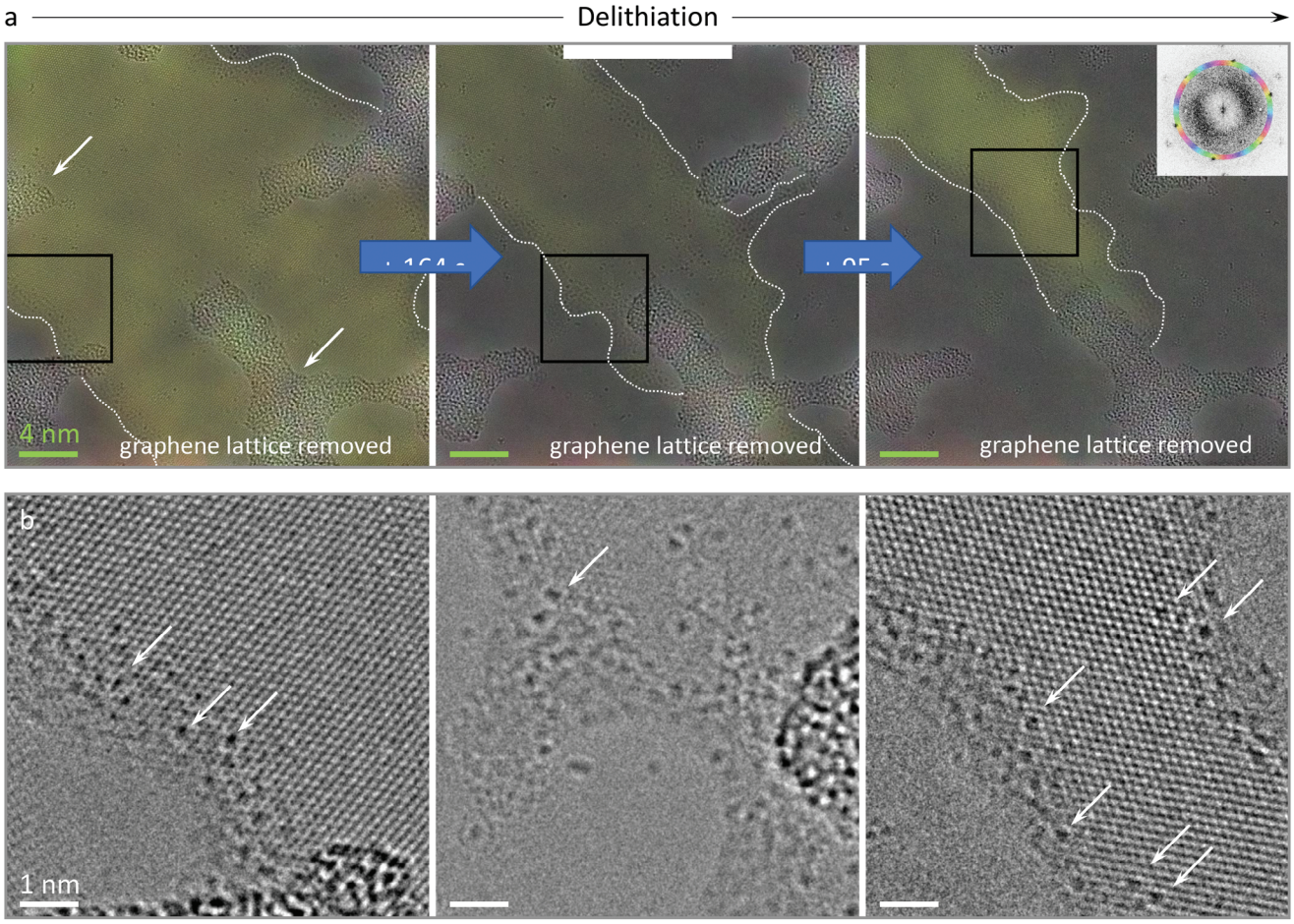


**Figure 7.** Observing delithiation at the atomic scale. a) A series of $C_C/C_S$-corrected HRTEM images with graphene lattice removed, recorded during another delithiation inside bilayer graphene. The edges of the Li crystal are highlighted by white dots. Two $Li_xO_y$ islands remaining from the previous cycle are marked by the arrows. Orientation maps of Li are overlaid. b) Magnified views of the boxed areas in (a). Many O atoms gather at the edges, some examples are marked by the arrows. The O atoms move with the edges as the Li crystal decreases in size.

material in the system as residual from the last cycle, some examples are marked by the arrows in Figure 7a. We found that the residual $Li_xO_y$ marked by the arrows kept its shape, indicating that the "trapped" Li was not active anymore in the delithiation process. During the following lithiation process, the residual amorphous $Li_xO_y$ acted as nucleation seeds in addition to the carbon vacancies (O has more available electrons and is easy to bond with Li, thus, Li crystals grew around the amorphous $Li_xO_y$), but the amorphous $Li_xO_y$ itself did not change anymore (see Video S3). Hence, we conclude that once residual $Li_xO_y$ forms, the Li bound in this $Li_xO_y$ could not be deinserted anymore and remained between the graphene sheets, which is also known as the formation of "dead lithium" – though this term has been commonly used for lithium oxide and lithium carbonate residues outside the electrode active material so far.[44,45] In fact, when continuing the cycling, more and more $Li_xO_y$ formed, immobilising an increasing fraction of Li in $Li_xO_y$ residuals, accumulating between the graphene layers.

## 3. Conclusion

In this work, we studied in detail how the nucleation and crystal formation take place during lithiation and delithiation into graphene sheets at the atomic scale using in situ spherical- and chromatic aberration-corrected transmission electron microscopy. Our detailed analysis of the TEM images and our theoretical study revealed that the Li crystals nucleate at carbon vacancies in graphene and grow further showing well-formed facets. We further identified the crystals as face-centered cubic (*fcc*) and observed single foreign oxygen atoms inside the crystals.

We find that the shape of the Li crystals often changes from faceted to irregular early in the delithiation process, and suggest that the foreign oxygen atoms play the key role. These oxygen atoms diffuse to the crystal surface and initially form only an amorphous lithium oxide rim. The crystals shrink during further delithiation, forming amorphous lithium oxide patches. When the lithium oxide forms, the lithium ions can no longer be

active in subsequent cycles, resulting in a loss of capacity during cycling.

## 4. Experimental Section

*Fabrication of the Custom-Made Device for (de)lithiation*: Nearly 200 sample carrier chips were prepared (see ref. [32] for fabrication details). Bi-/trilayer graphene, exfoliated from bulk natural graphite, was dry-transferred over the holes in the $Si_3N_4$ membrane on the custom-made TEM carrier chip, covering the electrical contacts made of either 60 nm-thick Ti or Pt. A drop of polymer electrolyte was casted on the chip, covering one edge of graphene and several selected contacts. The electrolyte was protected from outgassing into vacuum by covering a 200 nm-thick $SiO_x$ layer onto the surface of the electrolyte.

*In Situ TEM Measurements*: All the in situ TEM measurements were carried out using the $C_C/C_S$-corrected SALVE microscope (https://www.salve-project.de/) operated at 80 kV.[33] An FEI NanoEx-i/v in situ holder was used to provide a bias voltage into the custom-made chip. Prior to each lithiation experiment, the sample was current annealed using pre-fabricated electric contacts connected to the graphene flake, but not to the Li reservoir. This provided atomically clean and defect-free regions of free-standing graphene for the subsequent lithiation.[46] A constant voltage of $U_G = 5$ V was applied for lithiation, while $U_G = 0$ V was applied for delithiation. It has to be mentioned that only ≈1 out of 10 chips yielded in successful lithiation/delithiation experiments that could be observed either because of not working contacts or broken graphene flakes. For each functional chip, up to dozens of full cycles were probed until the contacts were broken due to the large current.

The overview images of lithiation and delithiation were recorded using a 4k × 4k FEI CETA2 CMOS camera. The exposure times were typically 1 s and the doses were in average $1 \times 10^6$ $e^-$ $nm^{-2}$. The images were acquired at 71 000 × magnification resulting in ca. 164 nm × 164 nm field of view. This setting allowed a good sampling of ca. 0.04 nm $pixel^{-1}$ with the possibility of HRTEM imaging (reflections of both graphene and Li were visible in FFT at the same time). However, a large underfocus had to be used to increase the contrast of Li at this magnification, so that behavior of Li could be noticed during the experiment. In general, lithiation was much faster than delithiation in our overview experiment. It took only several minutes to fully fill the graphene during lithiation, while it took up to hours for delithiation which resulted in damage of the sample by continues electron irradiation. Beam blanking was applied and dose rates ($1 \times 10^5$ $e^-$ $nm^{-2}$) were reduced to minimize electron beam damage when waiting during delithiation processes.

To record atomic resolved HRTEM images, $C_S$ was set to ca. −10 µm. However, it was difficult to judge the local defocus value when the graphene and Li crystals overlapped and only moiré patterns could be seen during the experiment. Therefore, defocus was always adjusted during the continuous recording at high magnification. All the HRTEM images were later Fourier filtered by removing the graphene (Li) lattice, leaving Li (graphene) lattice visible (see Figure S3, Supporting Information for an example). Only the filtered images with good quality, which were recorded coincidently with the correct defocus value for either Li or graphene, were used for further analysis at the atomic scale.

A Gatan Quantum ERS energy filter attached to the microscope was used for local EELS spectra. EELS spectra were acquired in diffraction mode using a typical probe of 200 nm width (slightly larger than the field of view). The dispersion of the spectrometer was 0.1 eV $pixel^{-1}$.

HRTEM image calculations were carried out with the following parameters: focal spread 0.5 nm, image spread 35 pm, convergence angle 0.2 mrad, $C_5 = 2.8$ mm, $C_3 = -8.74$ µm, optimum defocus 6 nm. The focal range were −20 nm to +20 nm around the optimum focus.

*Estimation of the Nucleation Density of Li at the Beginning of Lithiation*: The images of Figure 1a recorded at 0 s (shortly before the beginning of the lithiation) and 5 s (the first well-recorded image after the beginning of the lithiation) were used to estimate the nucleation density of Li. The images between 0 and 5 s were recorded with low quality and could not be used because the sample shortly drifted in the first 5 s due to the start of the biasing. A clean area in the original image at 0 s was selected so that the estimation of the nucleation density was independent of dirt or contamination. The number of the Li seeds (shown as dark patches in the image) were counted in the image at 5 s, and the nucleation density $D$ was then estimated by the following equation:

$$D = n_{seeds}/A \quad (1)$$

where $n_{seeds}$ is the number of the seeds in the field of view. $A$ is the area of the field of view.

*Orientation Mapping in the HRTEM Images of Li Crystals*: The ImageJ plugin OrientationMapping (https://github.com/mmohn/OrientationMapping) was used for the orientation mapping in the HRTEM images of Li crystals.[34] With this plugin, an RGB bandpass filter mask with a sixfold symmetry (the rotational symmetry was based on the symmetry of the Li crystals) was applied to the second order reflections of Li (the first order reflections are missing due to the *fcc* structure, as already described in the text) in the Fourier transform of the HRTEM images. The "number of orientations", which determines the number of segments per reflection, was set to 30 (thus, the resolution of orientation in the orientation maps was 2°), and a stack of 30 filter masks were created. Each mask was separately applied to the FFT of the original images, and the inverse FFT was then used to obtain the Fourier filtered images. Finally, colours were assigned to the RGB filtered images such that each orientation showed up with a different colour.

*Computational Details*: Density functional theory calculations were performed using the Perdew–Burke–Ernzerhof (PBE) exchange-correlation[47] functional as implemented in Vienna ab-initio Simulation Package (VASP).[48,49] The structures were relaxed with a force tolerance of 0.01 eV $Å^{-1}$ and electronic convergence criteria of $10^{-5}$ eV. The Brillouin zone of the *fcc*-Li and graphene primitive cells were sampled using (12 × 12 × 1) and (14 × 14 × 14) Monkhorst-Pack k-points, respectively. Additionally, van der Waals interactions were accounted for using the DFT-D2 method.[50]

The energetics of Li facets were assessed by evaluating the surface energy as:

$$E_{surface} = (E_{slab} - E_{bulk})/2A \quad (2)$$

where $E_{slab}$ and $E_{bulk}$ are the energies of the Li slab and bulk *fcc* phase, respectively. $A$ refers to the surface area.

The behavior of point defects at the graphene/Li interface and impurity atoms in Li crystals were studied by calculating their energetics using periodic supercells.[37]

The simulation model of the graphene/Li (111) interface was constructed using a 5 × 5 graphene supercell on top of a (111) 4 × 4 × 4 Li slab, with a total strain of ≈0.47%, containing 114 atoms. For the graphene/Li (100) interface, the structure includes a 7 × 2 graphene supercell on top of a (100) 4 × 2 × 4 Li slab, with a total strain of ≈0.54%, containing 60 atoms.

## Supporting Information

Supporting Information is available from the Wiley Online Library or from the author.

## Acknowledgements

The authors thank the German Research Foundation (DFG) through projects KR 4866/8-1 and the collaborative research centre "Chemistry of Synthetic 2D Materials" CRC-1415-417590517. Generous CPU time grants from the Technical University of Dresden computing cluster (TAURUS) and Gauss Centre for Supercomputing e.V. (www.gauss-centre.eu), Supercomputer HAWK at Höchstleistungsrechenzentrum Stuttgart (www.hlrs.de), are greatly appreciated. The

authors acknowledge financial support from the Helmholtz Association and the German Federal Ministry of Education and Research (BMBF) within the ExcellBattUlm project (03XP0257C and 03XP0257D).

Open access funding enabled and organized by Projekt DEAL.

## Conflict of Interest

The authors declare no conflict of interest.

## Data Availability Statement

The data that support the findings of this study are available in the supplementary material of this article.

## Keywords

atomic defects, bi-/trilayer graphene, DFT calculation, high-resolution transmission electron microscopy, in situ lithiation and delithiation

Received: April 9, 2024
Revised: June 13, 2024
Published online:

[1] M. Marinaro, D. Bresser, E. Beyer, P. Faguy, K. Hosoi, H. Li, J. Sakovica, K. Amine, M. Wohlfahrt-Mehrens, S. Passerini, *J. Power Sources* **2020**, *459*, 228073.
[2] Y. Miao, L. Liu, Y. Zhang, Q. Tan, J. Li, *J. Hazard. Mater.* **2022**, *425*, 127900.
[3] W. Li, H. Zhang, B. van Vlijmen, P. Dechent, D. U. Sauer, *Energy Storage Mater.* **2022**, *53*, 453.
[4] A. Masias, J. Marcicki, W. A. Paxton, *ACS Energy Lett.* **2021**, *6*, 621.
[5] J. S. Edge, S. O'Kane, R. Prosser, N. D. Kirkaldy, A. N. Patel, A. Hales, A. Ghosh, W. Ai, J. Chen, J. Yang, S. Li, M. C. Pang, L. Bravo Diaz, A. Tomaszewska, M. W. Marzook, K. N. Radhakrishnan, H. Wang, Y. Patel, B. Wu, G. J. Offer, *Phys. Chem. Chem. Phys.* **2021**, *23*, 8200.
[6] J. Vetter, P. Novák, M. R. Wagner, C. Veit, K. C. Möller, J. O. Besenhard, M. Winter, M. Wohlfahrt-Mehrens, C. Vogler, A. Hammouche, *J. Power Sources* **2005**, *147*, 269.
[7] C. Lin, A. Tang, H. Mu, W. Wang, C. Wang, *J Chem* **2015**, *2015*, 104673.
[8] X. G. Yang, Y. Leng, G. Zhang, S. Ge, C. Y. Wang, *J. Power Sources* **2017**, *360*, 28.
[9] J. A. Gilbert, I. A. Shkrob, D. P. Abraham, *J. Electrochem. Soc.* **2017**, *164*, A389.
[10] C. Zhan, T. Wu, J. Lu, K. Amine, *Energy Environ. Sci.* **2018**, *11*, 243.
[11] I. Laresgoiti, S. Käbitz, M. Ecker, D. U. Sauer, *J. Power Sources* **2015**, *300*, 112.
[12] F. A. Soto, A. Marzouk, F. El-Mellouhi, P. B. Balbuena, *Chem. Mater.* **2018**, *30*, 3315.
[13] X. M. Liu, C. B. Arnold, *J. Electrochem. Soc.* **2020**, *167*, 130519.
[14] Y. Zhang, L. Tao, C. Xie, D. Wang, Y. Zou, R. Chen, Y. Wang, C. Jia, S. Wang, *Adv. Mater.* **2020**, *32*, 1905923.
[15] R. Xu, K. Zhao, *J Mech Phys Solids* **2018**, *121*, 258.
[16] J. Cannarella, C. B. Arnold, *J. Electrochem. Soc.* **2015**, *162*, A1365.
[17] Y. Jia, B. Liu, Z. Hong, S. Yin, D. P. Finegan, J. Xu, *J. Mater. Chem. A* **2020**, *8*, 12472.
[18] G. Giuli, A. Trapananti, F. Mueller, D. Bresser, F. Dácapito, S. Passerini, *Inorg. Chem.* **2015**, *54*, 9393.
[19] G. Giuli, T. Eisenmann, D. Bresser, A. Trapananti, J. Asenbauer, F. Mueller, S. Passerini, *Materials (Basel)* **2017**, *11*, 49.
[20] J. Asenbauer, A. Hoefling, S. Indris, J. Tübke, S. Passerini, D. Bresser, *ACS Appl. Mater. Interfaces* **2020**, *12*, 8206.
[21] M. M. Rahman, W. Y. Chen, L. Mu, Z. Xu, Z. Xiao, M. Li, X. M. Bai, F. Lin, *Nat. Commun.* **2020**, *11*, 4548.
[22] A. Van Der Ven, C. Marianetti, D. Morgan, G. Ceder, *Solid State Ionics* **2000**, *135*, 21.
[23] J. Niu, R. Shao, J. Liang, M. Dou, Z. Li, Y. Huang, F. Wang, *Nano Energy* **2017**, *36*, 322.
[24] Q. Li, Z. Yao, E. Lee, Y. Xu, M. M. Thackeray, C. Wolverton, V. P. Dravid, J. Wu, *Nat. Commun.* **2019**, *10*, 2515.
[25] N. H. Vu, P. Arunkumar, J. C. Im, D. T. Ngo, H. T. T. Le, C. J. Park, W. Bin Im, *J. Mater. Chem. A* **2017**, *5*, 15730.
[26] M. Reynaud, J. Serrano-Sevillano, M. Casas-Cabanas, *Chem. Mater.* **2023**, *35*, 3345.
[27] J. Asenbauer, T. Eisenmann, M. Kuenzel, A. Kazzazi, Z. Chen, D. Bresser, *Sustain. Energy Fuels* **2020**, *4*, 5387.
[28] X. Fan, W. T. Zheng, J. L. Kuo, *ACS Appl. Mater. Interfaces* **2012**, *4*, 2432.
[29] D. Pan, S. Wang, B. Zhao, M. Wu, H. Zhang, Y. Wang, Z. Jiao, *Chem. Mater.* **2009**, *21*, 3136.
[30] R. Mukherjee, A. V. Thomas, D. Datta, E. Singh, J. Li, O. Eksik, V. B. Shenoy, N. Koratkar, *Nat. Commun.* **2014**, *5*, 3710.
[31] M. Kühne, F. Paolucci, J. Popovic, P. M. Ostrovsky, J. Maier, J. H. Smet, *Nat. Nanotechnol.* **2017**, *12*, 895.
[32] M. Kühne, F. Börrnert, S. Fecher, M. Ghorbani-Asl, J. Biskupek, D. Samuelis, A. V. Krasheninnikov, U. Kaiser, J. H. Smet, *Nature* **2018**, *564*, 234.
[33] M. Linck, P. Hartel, S. Uhlemann, F. Kahl, H. Müller, J. Zach, M. Haider, M. Niestadt, M. Bischoff, J. Biskupek, Z. Lee, T. Lehnert, F. Börrnert, H. Rose, U. Kaiser, *Phys. Rev. Lett.* **2016**, *117*, 076101.
[34] O. Lehtinen, H.-P. P. Komsa, A. Pulkin, M. B. Whitwick, M.-W. W. Chen, T. Lehnert, M. J. Mohn, O. V. Yazyev, A. Kis, U. Kaiser, A. V. Krasheninnikov, *ACS Nano* **2015**, *9*, 3274.
[35] J. C. Meyer, F. Eder, S. Kurasch, V. Skakalova, J. Kotakoski, H. J. Park, S. Roth, A. Chuvilin, S. Eyhusen, G. Benner, A. V. Krasheninnikov, U. Kaiser, *Phys. Rev. Lett.* **2012**, *108*, 196102.
[36] J. C. Meyer, F. Eder, S. Kurasch, V. Skakalova, J. Kotakoski, H. J. Park, S. Roth, A. Chuvilin, S. Eyhusen, G. Benner, A. V. Krasheninnikov, U. Kaiser, *Phys. Rev. Lett.* **2013**, *110*, 239902.
[37] X. Zhang, M. Ghorbani-Asl, Y. Zhang, A. V. Krasheninnikov, *Mater. Today Energy* **2023**, *34*, 101293.
[38] C. S. Barrett, *Phys. Rev.* **1947**, *72*, 245.
[39] S. Riikonen, A. V. Krasheninnikov, L. Halonen, R. M. Nieminen, *J. Phys. Chem. C* **2012**, *116*, 5802.
[40] X. Hu, T. Björkman, H. Lipsanen, L. Sun, A. V. Krasheninnikov, *J. Phys. Chem. Lett.* **2015**, *6*, 3263.
[41] M. Liu, A. Kutana, Y. Liu, B. I. Yakobson, *J. Phys. Chem. Lett.* **2014**, *5*, 1225.
[42] K. Doll, N. M. Harrison, V. R. Saunders, *J Phys Condens Matter* **1999**, *11*, 5007.
[43] J. L. Meijering, *Acta Metall.* **1955**, *3*, 157.
[44] J. Wandt, P. Jakes, J. Granwehr, R. A. Eichel, H. A. Gasteiger, *Mater. Today* **2018**, *21*, 231.
[45] K. S. N. Vikrant, E. McShane, A. M. Colclasure, B. D. McCloskey, S. Allu, *J. Electrochem. Soc.* **2022**, *169*, 040520.
[46] B. Westenfelder, J. C. Meyer, J. Biskupek, S. Kurasch, F. Scholz, C. E. Krill, U. Kaiser, *Nano Lett.* **2011**, *11*, 5123.
[47] J. P. Perdew, K. Burke, M. Ernzerhof, *Phys. Rev. Lett.* **1996**, *77*, 3865.
[48] G. Kresse, J. Furthmüller, *Phys Rev B Condens Matter Mater Phys* **1996**, *54*, 11169.
[49] D. Joubert, *Phys. Rev. B* **1999**, *59*, 1758.
[50] S. Grimme, *J. Comput. Chem.* **2006**, *27*, 1787.